A Unified Homogenization Framework for Straight- and Curved-Crease Origami Materials

MINGJIE LI, ETH Zürich, Switzerland
JUAN SEBASTIAN MONTES MAESTRE, ETH Zürich, Switzerland
EMILIEN GANIER, EPFL, Switzerland, and École Polytechnique, France
KLARA MUNDILOVA, EPFL, Switzerland
MARK PAULY, EPFL, Switzerland
BERNHARD THOMASZEWSKI, ETH Zürich, Switzerland

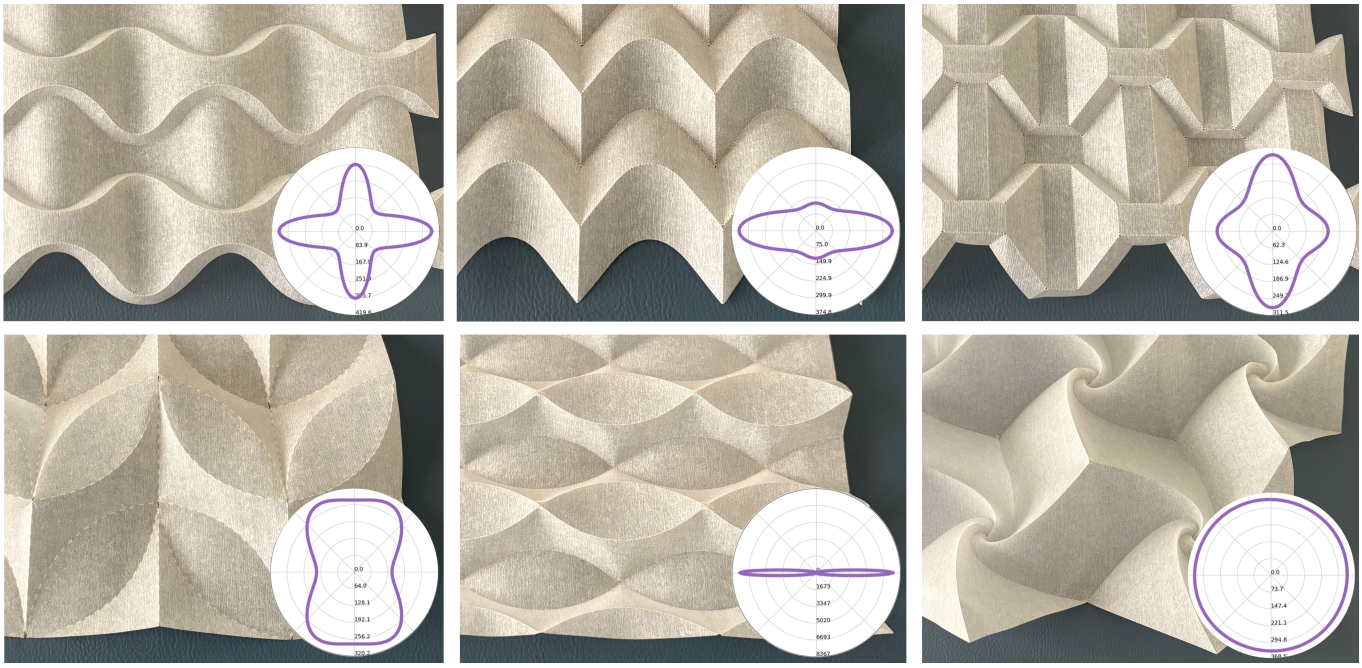

Fig. 1. Computational and physical exploration of periodic origami materials reveals a wide spectrum of effective material properties. The polar plots indicate orientation-dependent bending stiffness computed with our novel homogenization approach. The physical prototypes have been manually folded from plastified paper along crease curves pre-scored with a laser cutter.

We present a computational framework for numerical homogenization of origami materials—thin sheets structured with periodic crease patterns that, once folded, exhibit diverse and often unusual mechanical properties. Whereas the in-plane stiffness of conventional sheet materials is typically orders of magnitude larger than their resistance to bending, origami-based folding introduces geometric structure that can drastically reshape both bending and stretching behavior. However, predicting how a particular crease pattern gives rise to effective macroscopic properties remains challenging due to the complex coupling of crease geometry, folding kinematics, and surface deformations. In this work, we introduce a computational framework that integrates simulation-based folding and numerical homogenization to explore the relationship between crease pattern and effective material behavior. To describe the macromechanical response of origami materials, we employ a quadratic energy model based on Classical Laminate Theory, together with a simplified treatment of crease plasticity. Our unified representation accommodates both straight- and curved-crease designs, revealing a rich space of origami materials with diverse behavior. In particular, we examine how pattern symmetry governs material symmetries, demonstrating examples that span the full spectrum from perfectly isotropic to highly anisotropic membrane and bending responses. Our framework further enables controlled exploration of parameter variations, illustrating how geometric features such as crease curvature shape macroscopic mechanical behavior. We showcase the potential of this approach through a broad

Authors' Contact Information: Mingjie Li, ETH Zürich, Zürich, Switzerland, mingjli@ethz.ch; Juan Sebastian Montes Maestre, ETH Zürich, Zürich, Switzerland, juansebastian.montesmaestre@inf.ethz.ch; Emilien Ganier, EPFL, Switzerland, and École Polytechnique, Paris, France, emilien.ganier@polytechnique.edu; Klara Mundilova, EPFL, Lausanne, Switzerland, klara.mundilova@epfl.ch; Mark Pauly, EPFL, Lausanne, Switzerland, mark.pauly@epfl.ch; Bernhard Thomaszewski, ETH Zürich, Zürich, Switzerland, bthomasz@ethz.ch.

ACM 1557-7368/2026/7-ART147
https://doi.org/10.1145/3811301

set of examples, ranging from canonical straight-crease patterns such as Miura-ori to complex curved-crease tessellations. While a quantitative analysis is left for future work, we validate our homogenized descriptions against native-scale simulations and qualitatively compare deformation behaviors with real-world prototypes.

ACM Reference Format:
Mingjie Li, Juan Sebastian Montes Maestre, Emilien Ganier, Klara Mundilova, Mark Pauly, and Bernhard Thomaszewski. 2026. A Unified Homogenization Framework for Straight- and Curved-Crease Origami Materials. *ACM Trans. Graph.* 45, 4, Article 147 (July 2026), 16 pages. https://doi.org/10.1145/3811301

1 Introduction

Understanding how geometric structure shapes the mechanical response of thin sheets is a central problem in engineering, architecture, and material science. Thin materials such as paper, metal foils, or polymer films typically exhibit high resistance to in-plane stretching while offering comparatively little resistance to bending. Modifying this imbalance without increasing material thickness or weight is a longstanding challenge.

Origami-inspired patterning offers a geometric avenue for enriching the mechanical behavior of thin sheets. By introducing periodic crease networks into an initially flat surface, origami tessellations give rise to folded configurations with complex three-dimensional geometry. These folded structures can exhibit macromechanical responses that differ fundamentally from those of flat sheets, including strong variation in directional stiffness and coupling between bending and stretching. As a result, origami materials have attracted growing interest across disciplines ranging from mechanical metamaterials to deployable structures and architectural engineering [Islam et al. 2025; Li et al. 2019; Meloni et al. 2021].

Nevertheless, establishing a clear and systematic relationship between an origami crease pattern and the resulting effective mechanical behavior remains a significant challenge. The folded configuration of an origami sheet is the result of a complex interplay between crease geometry, folding kinematics, and the thin-shell mechanics of the underlying material. These factors interact in nontrivial ways, making it difficult to predict macroscopic behavior from crease pattern alone—in particular when moving beyond classical straight-crease patterns, where the folded surface remains piecewise planar, to curved-crease tessellations that lead to more general piecewise developable surfaces.

In this work, we present a computational framework for analyzing origami materials through the lens of numerical homogenization. To this end, we propose a novel folding algorithm that, building upon the concept of strain-space modes [Tang et al. 2024], introduces *crease modes* to achieve energetically-optimal folded states with low membrane strains and no spurious face bending. To describe the macromechanical response of these folded configurations, we propose an efficient homogenization approach that uses a quadratic energy model based on Classical Laminate Theory, enabling separate modeling of membrane and bending stiffness as well as explicit coupling between them.

A key feature of our approach is a unified treatment of both straight- and curved-crease designs. While previous studies have primarily focused on straight-crease patterns, curved creases considerably expand the geometric and mechanical vocabulary, introducing smoothly varying surface curvature and richer coupling between bending and in-plane deformation. Supporting both pattern classes within a single pipeline enables comparative analysis across a broad family of origami materials.

Using this framework, we investigate how symmetries in the crease pattern influence symmetries of the homogenized material response, revealing behaviors that range from perfectly isotropic to strongly anisotropic in both membrane and bending regimes. We further explore how continuous parameter variations—such as changes in crease curvature—affect macroscopic stiffness and deformation behavior. We demonstrate the capabilities of our approach through an extensive set of examples, spanning well-known straight-crease tessellations such as Miura-ori as well as families of curved-crease designs. Our homogenized models are validated against native-scale simulations, and we qualitatively compare predicted deformations with fabricated physical prototypes. We leave a quantitative analysis for future work.

Our source code and folding patterns are available at https://github.com/mingj1125/homogenizationorigami.

2 Related Work

Programmable Materials. With the widespread availability of 3D-printing technology, the analysis and design of metamaterials, whose tailored microstructures enable a broad range of macromechanical properties [Bertoldi et al. 2017], has become an active area of research in visual computing [Bickel et al. 2010]. While the initial focus was on three-dimensional materials [Martínez et al. 2016, 2017; Panetta et al. 2015; Schumacher et al. 2015], two-dimensional metasheets with programmable mechanical properties have recently seen increasing interest [Li et al. 2023; Martínez et al. 2019; Schumacher et al. 2018; Tozoni et al. 2020; Zhang et al. 2023]. Rather than just a simpler version of their 3D counterparts, the ability of metasheets to bend out of plane adds opportunities for control but also extra complexity. While some works deliberately separate stretching and bending responses [Montes Maestre et al. 2024; Schumacher et al. 2018; Tang et al. 2023], others account for coupling to a limited extent [Feng et al. 2024; Sperl et al. 2020]. For Origami plates, the interplay between membrane and bending deformations is a central characteristic and our method is able to capture the full coupling behavior.

Deployable Surfaces. Physical surfaces that deploy from a flat state to curved configurations have many applications. For example, through local control of pattern parameters, auxetic surfaces combine large expansion and double-curvature shapes [Konaković et al. 2016; Konaković-Luković et al. 2018]. Strategic placement of 3D-printed reinforcements onto pre-stretched membranes enables self-actuating surfaces that deploy into desired equilibrium shapes [Guseinov et al. 2017; Jourdan et al. 2022; Pérez et al. 2017]. Another line of work investigates the design of pneumatic surfaces that, through carefully designed tubes and channels, inflate into desired target shapes [He et al. 2025; Panetta et al. 2021; Ren et al. 2024]. As a common aspect between these works, evaluating the shape or performance of the deployed surfaces requires simulation,

i.e., the solution of a non-trivial minimization problem. Our setting likewise involves a complex nonlinear map, but rather than inflation or tension-based actuation, we simulate the progressive folding of the surface along tailored crease lines and curves.

Origami Tessellations. A class of deployable forms with a long-standing tradition in artistic expression is obtained by folding sheet materials along straight or curved-crease patterns. For engineering and architectural applications, folded geometries based on repeating unit cells are of particular importance, benefiting from simplified structures while still providing functional capabilities. One of the most prominent examples is the Miura-ori pattern [Koryo 1985], which has found widespread use in deployable structures, space applications, and mechanical metamaterials. Beyond Miura-ori, a large number of tessellated origami patterns have been developed; for a comprehensive list of references, see the work of Lang [2017].

Curved counterparts to straight-crease tessellations have also been a subject of exploration in origami. Early work by Huffman examines patterns composed of conic creases [Demaine et al. 2011], emphasizing their aesthetic appeal while laying the foundation for subsequent theoretical studies in curved-crease origami [Demaine et al. 2015, 2018]. Curved-crease tessellations continue to inspire contemporary origami artists, including Lukasheva [2021], Polly Verity, and Mitani [2019]. Leung and Garibi [2024] illustrate connections between straight-crease origami tessellations and their curved counterparts.

While artistic exploration produces intricate and expressive folded surfaces, their realization typically requires significant manual expertise. In particular, folding large-scale tessellations is time-consuming and nontrivial, motivating the use of computational design and simulation tools to explore, analyze, and automate the generation and folding of such structures. Our work contributes to the existing tool set with new folding and homogenization algorithms that, taken together, can predict the macromechanical behavior of origami tessellations before their physical realization.

Folding Simulation. Due to the high complexity of folding large origami patterns and tessellations, efficient folding simulation approaches are an active area of research. Notable examples for straight-crease origami include the software *Freeform Origami* by Tachi [2010] and its novel implementation as the Grasshopper for Rhino plugin *Crane* by Suto et al. [2023]. By using conforming discretizations, the accessible browser-based app *Origami Simulator*[1] by Ghassaei et al. [2018] can also handle curved creases. Beyond triangulations, other approaches simulate folded shapes using planar quad-dominant meshes [Kilian et al. 2008, 2017], B-spline patches [Tang et al. 2016], and discrete orthogonal geodesic nets [Rabinovich et al. 2019]. Building on the nonlinear eigenmodes introduced by Dünser et al. [2022], Tang et al. [2024] describe an automated approach for discovering energetically optimal folding transformations for thin-sheet materials using strain-space eigenmodes. However, their method produces soft folds and does not account for the effects of sharp curved or straight creases. In this work, we extend these methods to model curved folding within a simulation that produces energetically-optimal folded states, providing a strong and novel foundation for analyzing the mechanical properties of periodically folded origami sheets.

[1] see origamisimulator.org

Origami Materials. The mechanical behavior of origami tessellations has become an active area of research; see, e.g., the recent overview by Zhai et al. [2021]. Properties such as the Poisson ratios under membrane and bending deformations of well-known designs, including the Miura-ori and eggbox patterns, have been studied extensively [Lv et al. 2014; Schenk and Guest 2010, 2013; Wei et al. 2013]. Their ability to approximate curved surfaces has been investigated as well [Dudte et al. 2016; Nassar et al. 2017].

The stiffness-enhancing benefits of curved-crease origami tessellations have been studied, e.g., in the context of curved folded cores [Zakirov and Alekseyev 2004]. Subsequent studies have highlighted the role of curvature-induced geometric stiffness in thin-sheet structures, such as through increases in the second moment of area [Woodruff 2022; Woodruff and Filipov 2021]. Building on these ideas, Sun et al. [2024] investigate origami metamaterials composed of parallel curved creases and demonstrate programmable stiffness and stability characteristics arising from their geometry. With a similar motivation, Karami et al. [2024] explore a curved-crease variant of the Miura-ori pattern for morphing metamaterials, examining how crease geometry influences their Poisson's ratios. Complementary theoretical developments include Lagrangian formulations and group orbit–based approaches for their computation [Liu and James 2025]. Combinations of curved- and straight-creases enable the design of origami materials with programmable multistability, as demonstrated in recent work by Chai et al. [2024].

Perhaps most closely related to our work is the recent study by Vasudevan and Pratapa [2024], who likewise adopt a homogenization-based framework to characterize the mechanics of origami tessellations. Their approach, however, relies on a simplified mechanical model that effectively restricts the analysis to rigidly foldable patterns composed of straight creases—they concentrate on the Miura-ori pattern and a variant thereof. In contrast, our method accurately captures facet curvature induced by bending along curved creases, enabling the analysis of a substantially broader class of tessellations that combine straight and curved crease geometries. This level of generality allows for a systematic investigation of the interplay between crease pattern geometry and effective material symmetry. In particular, we demonstrate examples exhibiting isotropic, tetragonal, orthotropic, and fully anisotropic mechanical behavior.

3 Overview

We present a computational framework for modeling and analysis of periodic origami materials made from flat sheets folded along straight or curved creases (see Fig. 1). We focus on periodic crease patterns that fold into structured plates that can be characterized by a planar mid-surface in the folded configuration.

We first introduce our new approach for computing energetically-optimal folded configurations for periodic origami patterns based on a unit-cell approach (Sec. 4). To determine the macromechanical bending and stretching properties of the resulting origami materials, we describe an efficient homogenization approach based on Classical Laminate Theory (Sec. 5). We then analyze the homogenization

results for a diverse set of example patterns and study relations between mechanical behavior and crease layout symmetries (Sec. 6). Finally, we show physical prototypes for selected patterns and qualitatively compare their mechanical behavior with our homogenized simulations. We conclude with a discussion of limitations and some directions for future research.

4 Folding

To characterize the mechanical behavior of origami materials, we must be able to accurately predict folded configurations for given crease layouts. Since origami materials are made from quasi-inextensible sheets, the folding simulation must generate configurations with very low in-plane strain while reproducing realistic face curvatures. To achieve this, we introduce a simulation method that enforces a target folding magnitude while minimizing the sheet's elastic energy. Before describing the method, we briefly summarize our unit-cell model, including the crease pattern, boundary conditions, and underlying mechanical model.

4.1 Unit-Cell Model

The input to our method is a periodic crease pattern defined on a parallelogram-shaped unit cell. The crease pattern consists of a set of crease segments, either curved or straight, that induce a set of faces. Mountain-valley assignments indicate whether a crease should bend up or down during folding.

We triangulate the unit cell and its creases into a periodic mesh as shown in Fig. 2 (*left*). Let $\mathbf{X}$ and $\mathbf{x}$ denote the vertex positions for the rest and deformed configurations, respectively. As the unit cell deforms during folding, its boundaries must remain periodic. This periodicity implies that corresponding vertex pairs, $(\mathbf{x}_i^u, \mathbf{x}_j^u)$ and $(\mathbf{x}_i^v, \mathbf{x}_j^v)$, on opposite cell boundaries in the u and v direction must satisfy

$$\mathbf{x}_i^u - \mathbf{x}_j^u = \mathbf{t}^u \quad \text{and} \quad \mathbf{x}_i^v - \mathbf{x}_j^v = \mathbf{t}^v \,, \tag{1}$$

where $\mathbf{t}^u$ and $\mathbf{t}^v$ are the tiling vectors of the deformed cell.

Simulation Model. We use a standard discrete shell model for simulation, combining constant strain triangle finite elements for membrane deformations with a bending energy based on a per-triangle discretization of the shape operator [Grinspun et al. 2006].

Pre-scored patterns are easy to fold along creases but show stronger resistance to bending otherwise. To model this difference in bending stiffness, we modify the shape operator for triangles adjacent to creases.

Fig. 2. Unit-cell model. *Left*: Periodic triangle mesh conforming to crease pattern with mountain-valley assignments indicated in *red* and *blue*, respectively. *Middle*: simulation result for folded configuration. *Right*: corresponding physical prototype with pre-scored creases.

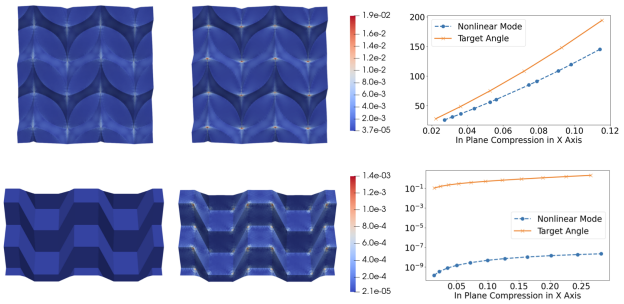

Fig. 3. Comparison between different folding simulation methods on two patterns. Our nonlinear folding modes (*left*) show lower peak strain compared to the penalty method with prescribed target angles (*middle*). This leads to substantially lower total elastic energy as shown in the corresponding plots on the right.

The shape operator is defined on a given center triangle and its three edge-adjacent neighbor triangles (*flaps*) as

$$\Lambda = \sum_{i=1}^{3} \frac{\theta_i}{2\bar{A}\bar{l}_i} \bar{\boldsymbol{d}}_i \bar{\boldsymbol{d}}_i^T \,, \tag{2}$$

where θ_i is the current dihedral angle between the center triangle and its i-th flap. All other quantities refer to the undeformed configuration: $\bar{A}$ is the center triangle's area, $\bar{l}_i$ is the length of edge i, and $\bar{\boldsymbol{d}}_i$ is a vector in the plane of the center triangle, orthogonal to edge i, pointing outward, and with magnitude equal to l_i. To modify the shape operator such that bending across crease edges is no longer penalized, we simply set $\theta_i = 0$ for the corresponding edge. Having removed bending resistance across creases in this way, we introduce hinge elements [Grinspun et al. 2003] for all crease edges, allowing us to selectively control their stiffness and rest angles during folding simulation and homogenization.

4.2 Folding Simulation

Given a periodic unit-cell mesh conforming to a set of creases, our goal is to compute the corresponding folded configuration. Although we typically know the sign of each crease angle, given as part of the input, the optimal angle magnitudes are not known *a priori*. Simply prescribing per-crease target angles generally leads to suboptimal results with excessive face bending or unacceptable membrane strains; see Fig. 3 for an example.

Intuitively, we would like to achieve a given folding progress—measured using an appropriate metric—with the least mechanical work. Following Dünser et al. [2022], we start in vertex space and ask for nodal displacements $\mathbf{u}$ of unit magnitude that induce the least energy. Approximating the energy of the sheet with a quadratic model, $E(\mathbf{u}) = \frac{1}{2}\mathbf{u}^T\mathbf{H}\mathbf{u}$, leads to a constrained optimization problem of the form

$$\min_{\mathbf{u}} \quad \frac{1}{2}\mathbf{u}^T\mathbf{H}\mathbf{u} \quad \text{s.t} \quad \frac{1}{2}(\mathbf{u}^T\mathbf{M}\mathbf{u} - 1) = 0 \,, \tag{3}$$

where we use the diagonal mass matrix $\mathbf{M}$ to obtain a resolution- and mesh-independent norm constraint. The first-order optimality

conditions of the above optimization problem are

$$\mathbf{Hu} - \lambda \mathbf{Mu} = \mathbf{0}\,, \tag{4}$$

where λ is a Lagrange multiplier. This expression shows that energetically optimal displacements correspond to the generalized eigenmodes of the energy Hessian $\mathbf{H}$. We solve the above generalized eigenvalue problem for a fixed number of eigenmodes $\mathbf{v}_i$ using the sparse algebra package Spectra[2].

For homogeneous, unstructured thin plates, the eigenvectors for the smallest (nonzero) eigenvalues correspond to smooth bending deformations, since bending is energetically much less expensive than stretching. To further encourage bending along creases, we set their stiffness to zero before computing eigenvectors. As a result, the lowest-order eigenmodes tend to concentrate bending along creases while adding curvature to faces as needed to prevent stretching.

Extension to Finite Deformations. Eigenmodes provide a tangent direction for the folding path, but simply following them would induce unacceptable stretching. To extend these modes to the finite-deformation regime, we follow Tang et al. [2024] and first map the vertex-space eigenvectors $\mathbf{v}_i$ into crease-angle space to obtain the *crease modes*

$$\mathbf{c}_i = \mathbf{J}\mathbf{v}_i\,, \quad \text{where} \quad \mathbf{J} = \frac{\partial \boldsymbol{\theta}}{\partial \mathbf{x}}\,, \tag{5}$$

and $\boldsymbol{\theta}$ denotes the vector of all crease angles. The crease modes provide first-order optimal directions for crease angle evolution. Instead of prescribing per-angle targets as in Tang et al. [2024], we impose the relaxed requirement that the folding path $\mathbf{x}(t)$ must make steady progress along the selected crease mode, i.e.,

$$\mathbf{c}^T \boldsymbol{\theta}(\mathbf{x}(t)) = \beta(t), \tag{6}$$

where $\beta(t)$ describes the folding progress. We then seek a folding trajectory that advances by a desired amount while minimizing elastic energy. In a time-discrete formulation, this naturally leads to the constrained optimization problem

$$\mathbf{x}_{n+1} = \mathbf{x}_n + \arg\min_{\Delta \mathbf{x}} E(\mathbf{x}_n + \Delta \mathbf{x}) \quad \text{s.t.} \quad \mathbf{c}^T \boldsymbol{\theta}(\mathbf{x} + \Delta \mathbf{x}) = \beta_{n+1}\,. \tag{7}$$

Since accurate satisfaction of the progress constraint is not critical, we replace it with a corresponding penalty term and solve a simpler unconstrained minimization problem,

$$\mathbf{x}_{n+1} = \mathbf{x}_n + \arg\min_{\Delta \mathbf{x}} E(\mathbf{x}_n + \Delta \mathbf{x}) + \frac{k_p}{2}(\mathbf{c}^T \Delta\boldsymbol{\theta}(\Delta \mathbf{x}) - \Delta\beta)^2\,, \tag{8}$$

where $\Delta\boldsymbol{\theta}(\Delta \mathbf{x}) = \boldsymbol{\theta}(\mathbf{x} + \Delta \mathbf{x}) - \boldsymbol{\theta}(\mathbf{x})$, $k_p = 1.0$ is a penalty coefficient, and $\Delta\beta$ is a user-provided step size. In our examples, we set $\Delta\beta = s|\mathbf{c}|^2$, where $s = 30.0$ is a scaling factor. To preserve periodicity during folding, we add tiling vectors as degrees of freedom and enforce (1) through variable elimination.

Discussion. While our method shares conceptual similarities with the approaches of Dünser et al. [2022] and Tang et al. [2024], several key differences enable our simulation to discover folded states with significantly lower elastic energy. Penalty-based strategies that rely on prescribing per-crease target angles of fixed magnitude generally fail to produce realistic folding behavior (see Fig. 3). Employing the modal folding method of Tang et al. [2024] to infer individual target angles for each crease only partially alleviates the issue: per-crease target angles inherently over-constrain the system, preventing it from settling into low-energy configurations. In contrast, the single-constraint formulation of Dünser et al. [2022] leaves substantially more flexibility for energy minimization. However, as reported by Tang et al. [2024], their vertex-space formulation introduces undesirable stretching for larger displacements. By combining crease-space eigenvectors with a single-constraint formulation, our approach is able to generate folded configurations with virtually no in-plane deformations, smooth face bending, and minimal elastic energy; see Fig. 3.

[2]https://spectralib.org/

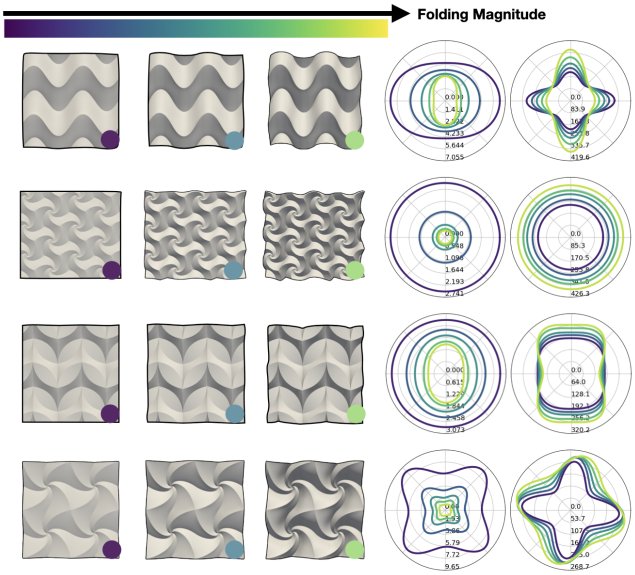

Fig. 4. Impact of folding magnitude on membrane and bending stiffness. The colors of the dots overlaid on the unit cells correspond to the curves in the stiffness plots.

5 Homogenization

Given a folded state of an origami material produced by our simulation method (Sec. 4), we aim to characterize its macroscopic bending and stretching response. To this end, we assume that all creases have undergone fully plastic deformation and therefore reset their rest angles to the current configuration. We additionally reset the crease bending stiffness to the material's default value.

To abstract away the geometric complexity of origami materials, we model their effective mechanical response using Kirchhoff plate theory. Specifically, we employ Classical Laminate Theory (CLT), which captures the influence of material and structural variations through the thickness [Reddy 2003]. For simplicity, we consider only the initial stiffness, i.e., the linear relationship between membrane and bending strains and the associated stresses and moments about the initial folded configuration. In this regime, a quadratic energy approximation based on CLT is sufficient.

5.1 Plate Model

We briefly recall the kinematics of Kirchhoff plates, then describe how these lead to corresponding stress–strain relationships.

Kirchhoff Plate Kinematics. A plate is a thin, three-dimensional body parameterized by a two-dimensional mid-surface, which we take to lie at $z = 0$. Kirchhoff plate theory assumes that lines initially normal to the mid-surface remain straight, normal, and unstretched during deformation. Consequently, there are no strains or stresses in the thickness direction, and transverse shear strains likewise vanish. Each material layer therefore experiences a plane state of strain and stress. Under these assumptions, the displacement field of the plate, $\mathbf{u}(x, y, z) = (u, v, w)^T$, takes the form

$$\begin{aligned} u(x, y, z) &= u_0(x, y) - z\frac{\partial w}{\partial x}\,, \\ v(x, y, z) &= v_0(x, y) - z\frac{\partial w}{\partial y}\,, \text{and} \\ w(x, y, z) &= w(x, y)\,, \end{aligned}$$

where (u_0, v_0) are in-plane displacements of the mid-surface and w is the transverse displacement in the normal direction. With the usual differential relations, the membrane strains take the form

$$\varepsilon_{xx}(x, y, z) = \frac{\partial u_0}{\partial x} - z\frac{\partial^2 w}{\partial x^2}\,, \tag{9}$$

$$\varepsilon_{yy}(x, y, z) = \frac{\partial v_0}{\partial y} - z\frac{\partial^2 w}{\partial y^2}\,, \quad \text{and} \tag{10}$$

$$\varepsilon_{xy}(x, y, z) = \frac{1}{2}\left(\frac{\partial u_0}{\partial y} + \frac{\partial v_0}{\partial x}\right) - z\frac{\partial^2 w}{\partial x \partial y}\,. \tag{11}$$

These three strain fields, which define the deformation at any point in the plate, can be compactly rewritten as

$$\boldsymbol{\varepsilon}(x, y, z) = \boldsymbol{\varepsilon}^0(x, y) + z\boldsymbol{\kappa}(x, y)\,, \tag{12}$$

where the mid-surface strains are given as

$$\boldsymbol{\varepsilon}^0(x, y) = (\varepsilon_{xx}(x, y, 0), \varepsilon_{yy}(x, y, 0), \varepsilon_{xy}(x, y, 0))^T\,, \tag{13}$$

and the bending strains or *curvatures* are

$$\boldsymbol{\kappa}(x, y) = (\kappa_{xx}, \kappa_{yy}, \kappa_{xy})^T = -\left(\frac{\partial^2 w}{\partial x^2}, \frac{\partial^2 w}{\partial y^2}, 2\frac{\partial^2 w}{\partial x \partial y}\right)^T\,. \tag{14}$$

Stiffness. For composite plates, each layer generally possesses its own in-plane stiffness matrix $\mathbf{C}(z) \in \mathbb{R}^{3\times3}$, which relates membrane strains to the corresponding in-plane stresses via $\boldsymbol{\sigma}(z) = \mathbf{C}(z)\,\boldsymbol{\varepsilon}(z)$. The effective stiffness of the plate is obtained by integrating these layerwise contributions through the thickness,

$$\mathbf{A} = \int_{-\frac{h}{2}}^{+\frac{h}{2}} \mathbf{C}(z)\,dz\,, \quad \mathbf{B} = \int_{-\frac{h}{2}}^{+\frac{h}{2}} z\mathbf{C}(z)\,dz\,, \quad \mathbf{D} = \int_{-\frac{h}{2}}^{+\frac{h}{2}} z^2\mathbf{C}(z)\,dz\,,$$

where $\mathbf{A}$ and $\mathbf{D}$ are symmetric 3×3 matrices representing the membrane and bending stiffnesses, respectively. The matrix $\mathbf{B}$, which is generally non-symmetric, characterizes the coupling between membrane strains and bending curvatures.

Summarizing membrane and bending strains at the midsurface as

$$\mathbf{s} = (\varepsilon^0_{xx}, \varepsilon^0_{yy}, 2\varepsilon^0_{xy}, \kappa_{xx}, \kappa_{yy}, \kappa_{xy})^T\,, \tag{15}$$

the energy density of the plate can be compactly written as

$$E_{\text{CLT}} = \frac{1}{2}\mathbf{s}^T\mathbf{K}\mathbf{s}\,, \quad \text{where} \quad \mathbf{K} = \begin{bmatrix} \mathbf{A} & \mathbf{B} \\ \mathbf{B}^T & \mathbf{D} \end{bmatrix}\,. \tag{16}$$

5.2 Plate Homogenization

Due to their complex structure, we cannot perform integration through the thickness in closed form for origami materials. We instead resort to numerical homogenization and probe a single unit cell with a set of six macro-level displacement fields,

$$\begin{aligned} \bar{\mathbf{u}}_1 &= (sx, 0, 0)^T & \bar{\mathbf{u}}_4 &= (-bxz, 0, \tfrac{1}{2}bx^2)^T \\ \bar{\mathbf{u}}_2 &= (0, sy, 0)^T & \bar{\mathbf{u}}_5 &= (0, -byz, \tfrac{1}{2}by^2)^T \\ \bar{\mathbf{u}}_3 &= (\tfrac{1}{2}sy, \tfrac{1}{2}sx, 0)^T & \bar{\mathbf{u}}_6 &= (-byz, -bxz, \tfrac{1}{2}bxy)^T\,, \end{aligned}$$

where the scalars s and b control the magnitude of membrane and bending strains, respectively. From Eqs. (9-11) and (14), it can be seen that $\bar{\mathbf{u}}_1$ to $\bar{\mathbf{u}}_3$ induce pure stretching and shearing (without bending), whereas $\bar{\mathbf{u}}_4$ to $\bar{\mathbf{u}}_6$ generate pure bending and torsion (without stretching the mid-surface).

Simply imposing these macroscopic displacement fields on the unit cell would overestimate the energy, as the resulting internal forces would not, in general, be in equilibrium at the interior nodes. We therefore introduce microscopic displacement fields $\tilde{\mathbf{u}}$ that allow internal nodes to adjust their positions so as to minimize the total energy,

$$E(\mathbf{u}) = \frac{1}{2}\mathbf{u}^T\mathbf{H}\mathbf{u} = \frac{1}{2}\tilde{\mathbf{u}}^T\mathbf{H}\tilde{\mathbf{u}} + \bar{\mathbf{u}}^T\mathbf{H}\tilde{\mathbf{u}} + E(\bar{\mathbf{u}})\,, \tag{17}$$

where $\mathbf{u} = \bar{\mathbf{u}} + \tilde{\mathbf{u}}$ is the total displacement field. To ensure that the prescribed macroscopic deformation, represented by $\bar{\mathbf{u}}_i$, is satisfied on average, we impose zero-mean conditions on $\tilde{\mathbf{u}}$. The corresponding three linear constraints, one per component, are enforced using Lagrange multipliers $\boldsymbol{\lambda}$. We additionally enforce periodicity on the microscopic displacements by eliminating variables.

Minimizing (17) subject to the zero-mean constraints leads to a constrained optimization problem, whose first-order optimality conditions give rise to the linear system

$$\begin{bmatrix} \mathbf{H} & \nabla\mathbf{C}^T \\ \nabla\mathbf{C} & \mathbf{0} \end{bmatrix} \begin{bmatrix} \tilde{\mathbf{u}} \\ \boldsymbol{\lambda} \end{bmatrix} = \begin{bmatrix} -\mathbf{H}\bar{\mathbf{u}} \\ \mathbf{0} \end{bmatrix}\,. \tag{18}$$

Solving this system yields the energetically optimal microscopic displacements $\tilde{\mathbf{u}}$. The six total displacement fields $\mathbf{u}_i = \bar{\mathbf{u}}_i + \tilde{\mathbf{u}}_i$ obtained in this way define a basis for first-order optimal plate deformations, from which we construct a quadratic macroscopic energy model. To this end, we use the Hill-Mandel condition [Hill 1963; Mandel 1971] and ask that microscopic and macroscopic energies should match. Since both macro- and microscopic energies are quadratic functions, we simply have

$$\mathbf{e}_j\mathbf{K}\mathbf{e}_i = \mathbf{u}_j^T\mathbf{H}\mathbf{u}_i \quad \forall i, j\,, \tag{19}$$

where $\mathbf{K}$ is the macroscopic stiffness matrix and $\mathbf{e}_k \in \mathbb{R}^6$, with $\mathbf{e}_{kl} = \delta_{kl}$, are coefficient vectors that induce unit strains along their corresponding microscopic displacement fields $\mathbf{u}_k$. The entries of the macroscopic stiffness matrix $\mathbf{K}$ then follow as

$$K_{ij} = \mathbf{u}_j^T\mathbf{H}\mathbf{u}_i\,. \tag{20}$$

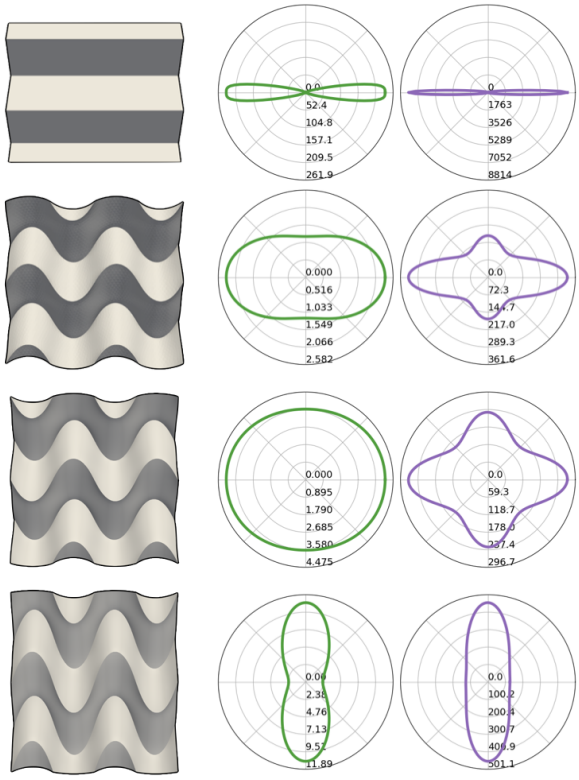

Fig. 5. Impact of changing crease curvature (*left*) on the directional membrane (*middle*) and bending (*right*) stiffness of the curved-crease sine wave pattern.

The 21 combinations obtained in this way are mapped to the three blocks of the stiffness matrix (16) as

$$A_{ij} = K_{ij}, \quad D_{ij} = K_{(i+3)(j+3)}, \quad \text{and} \quad B_{ij} = K_{i(j+3)}\,, \tag{21}$$

for $i, j \in \{1, 2, 3\}$.

Discussion. The macroscopic fields used for homogenization warrant some additional discussion. While the membrane modes $\bar{\mathbf{u}}_1$ to $\bar{\mathbf{u}}_3$ are valid irrespective of deformation magnitude, the bending modes, $\bar{\mathbf{u}}_4$ and $\bar{\mathbf{u}}_5$, only approximate cylindrical curvature. Nevertheless, they are perfectly periodic and remain valid for small displacements. The torsion mode $\bar{\mathbf{u}}_6$, however, violates two key assumptions: it is not periodic, and it introduces Gaussian curvature. For the latter, the associated inconsistency scales quadratically with the torsion amplitude γ. It is therefore negligible for sufficiently small displacements. The lack of periodicity, on the other hand, introduces an error that depends on the unit-cell size and influences the effective torsional stiffness. As a result, the homogenized response is not fully resolution independent. Similar observations have been made by Sperl et al. [2020] and Tang et al. [2023]. Nonetheless, the proposed approach enables a fully linear treatment of the problem, and our experiments across different cell sizes indicate that the resulting discrepancy is not severe. We therefore accept this trade-off and leave a more detailed investigation for future work.

5.3 Analysis

Within the validity of the quadratic energy model, the macroscopic stiffness matrix $\mathbf{K}$ fully characterizes the mechanical behavior of a homogenized origami plate. Although complete, this representation is not always intuitive for interpreting directional behavior. To provide a more accessible description, we compute directional stiffness profiles and the associated Poisson ratios by imposing uniaxial membrane and bending deformations. Because our primary interest is in predicting the *natural* response of origami materials—for example, during manual interaction—we seek deformation states that achieve a prescribed magnitude in a given direction α with minimal energy. This requirement leads to the optimization problem

$$\min_{\mathbf{s}} \ \frac{1}{2}\mathbf{s}^T\mathbf{K}\mathbf{s} \quad \text{s.t.} \quad \mathbf{c}(\alpha)^T\mathbf{s} = m\,, \tag{22}$$

where $\mathbf{s} = (\varepsilon_{xx}, \ldots, \kappa_{xy})^T$ is the strain vector and $\mathbf{c}(\alpha)$ models a linear constraint on the uniaxial deformation with direction α and magnitude m. The constraints for uniaxial bending and stretching in direction α take the form

$$\mathbf{c}_{\text{mem}}(\alpha) = (\cos^2\alpha, \sin^2\alpha, \cos\alpha\sin\alpha, 0, 0, 0)\,, \tag{23}$$

$$\mathbf{c}_{\text{bend}}(\alpha) = (0, 0, 0, \cos^2\alpha, \sin^2\alpha, \cos\alpha\sin\alpha)\,, \tag{24}$$

respectively. Since both expressions are linear equality constraints for fixed α and the objective is quadratic, optimization problem (22) admits a closed form solution,

$$\mathbf{s}^*(\alpha) = \mathbf{K}^{-1}\mathbf{c}(\alpha)[\mathbf{c}(\alpha)^T\mathbf{K}^{-1}\mathbf{c}(\alpha)]^{-1}m\,. \tag{25}$$

See also Appendix A. The energy associated with this optimal uniaxial deformation is

$$E^* = \frac{1}{2}(\mathbf{s}^*)^T\mathbf{K}\mathbf{s}^* = \frac{1}{2}(\mathbf{c}(\alpha)\mathbf{K}^{-1}\mathbf{c}(\alpha)^T)^{-1}m^2 = \frac{1}{2}k^*(\alpha)m^2\,, \tag{26}$$

where the generalized directional stiffness is defined as

$$k^*(\alpha) = \frac{1}{\mathbf{c}(\alpha)^T\mathbf{K}^{-1}\mathbf{c}(\alpha)}\,. \tag{27}$$

It is worth noting that, if restricted to stretching only, this directional stiffness is equivalent to the expression derived by Schumacher et al. [2018], who treat bending and stretching separately. Our formulation accounts for coupling between stretching and bending, which is an important characteristic of origami materials.

Using expression (27), we generate directional stiffness plots for homogenized origami materials. We furthermore compute corresponding directional Poisson ratios for membrane and bending deformations as

$$\nu_{\text{mem}}(\alpha) = -\frac{\varepsilon(\alpha + \frac{\pi}{2})}{\varepsilon(\alpha)}\,, \quad \nu_{\text{bend}}(\alpha) = -\frac{\kappa(\alpha + \frac{\pi}{2})}{\kappa(\alpha)}\,. \tag{28}$$

Finally, in order to quantify the coupling strength between stretching and bending, we use the energetically-optimal deformation $\mathbf{s}^*(\alpha)$ for an imposed unit stretch in direction α and measure the curvature induced by $\mathbf{s}^*(\alpha)$ as

$$\eta(\alpha) = \sqrt{\kappa_{xx}(\alpha)^2 + \kappa_{yy}(\alpha)^2 + 2\kappa_{xy}(\alpha)^2}\,. \tag{29}$$

The resulting set of polar plots provides a concise, interpretable summary of the macromechanical behavior of origami materials. We use this description as a basis for our analysis in Sec. 6.

6 Results

We evaluate our method on a diverse set of straight- and curved-crease patterns. These include origami patterns inspired by Ekaterina Lukasheva, such as spiral and leafy tessellations [Lukasheva 2021], David Huffman's lens tessellation and a conic crease pattern based on parabolas [Koschitz 2014], and Jun Mitani's tri-wing boomerang design and its variations [Mitani 2019]. Our experiments indicate a rich space of mechanical behavior, which we discuss in the following. We first investigate the mechanical spectrum of origami materials, focusing on material symmetries and how they relate to symmetries in the pattern. We then study the geometric relations that govern the stretching-bending coupling for origami materials. Furthermore, we explore the continuous parameter space of curved crease patterns and investigate how parameter changes affect material behavior. Finally, we compare simulation results obtained with our homogenized model to native-scale simulations and to deformations observed in physical prototypes.

6.1 Material Diversity

The crease patterns we investigate lead to origami materials with a wide range of mechanical behavior, ranging from perfect isotropy to complete anisotropy. As with other elastic media, these material symmetries are governed by pattern symmetries [Saxcé and Vallée 2013; Schumacher et al. 2018]. We discuss the relevant classes in the following.

Isotropic Materials. A six-fold and three-fold rotational symmetry of a pattern implies that the material behaves the same in every direction and is therefore isotropic. In this case, the behavior is determined by two independent constants (e.g., Young's modulus and Poisson's ratio) and the elasticity matrix takes the form

$$\mathbf{A}_{\text{iso}} = \begin{bmatrix} C_{11} & C_{12} & 0 \\ C_{12} & C_{11} & 0 \\ 0 & 0 & \frac{1}{2}(C_{11} - C_{12}) \end{bmatrix}. \tag{30}$$

As can be seen in Fig. 9 and 10, all six- and three-fold rotationally symmetric crease patterns lead to isotropic behavior for both stretching and bending.

Tetragonal Materials. A four-fold rotational symmetry of a pattern implies that the material behavior is identical in two orthogonal directions and thus *tetragonal*. Tetragonal materials are defined by three independent constants, and the elasticity matrix takes the form

$$\mathbf{A}_{\text{tetra}} = \begin{bmatrix} C_{11} & C_{12} & 0 \\ C_{12} & C_{11} & 0 \\ 0 & 0 & C_{33} \end{bmatrix}, \tag{31}$$

where $C_{33} \neq \frac{1}{2}(C_{11} - C_{12})$ in general. We can see in Fig. 9 and 10 that the crease patterns in this symmetry class indeed show tetragonal behavior for both stretching and bending.

Orthotropic Materials. If a pattern exhibits reflection symmetry with respect to one or two orthogonal axes, the resulting homogenized material behavior is orthotropic. In this case, the material possesses two perpendicular principal directions along which the stiffness may differ, but due to reflection symmetry there is no coupling between normal and shear responses. Consequently, the elasticity matrix of an orthotropic material contains four independent constants and takes the form

$$\mathbf{A}_{\text{ortho}} = \begin{bmatrix} C_{11} & C_{12} & 0 \\ C_{12} & C_{22} & 0 \\ 0 & 0 & C_{33} \end{bmatrix}. \tag{32}$$

As illustrated in Figs. 9-11, most of the examples we study fall into this category. While the majority of these orthotropic origami materials share the same symmetry axes for stretching and bending, a noteworthy exception are the discrete and continuous *Leafy* designs[3] shown in Fig. 10, rows *3* and *4* . For these patterns, the axes of symmetry that govern the membrane stiffness align with the horizontal and vertical directions. While the twofold reflection symmetry of the bending stiffness profile implies orthotropy, the corresponding principal axes differ from those of the membrane stiffness.

Anisotropy. If a pattern is only invariant to 180° rotation or has no symmetry at all, its mechanical behavior must be fully anisotropic. In this case, the material has six independent constants and the structure of the elasticity matrix becomes

$$\mathbf{A}_{\text{aniso}} = \begin{bmatrix} C_{11} & C_{12} & C_{13} \\ C_{12} & C_{22} & C_{23} \\ C_{13} & C_{23} & C_{33} \end{bmatrix}. \tag{33}$$

To verify this prediction, we consider a skewed version of the curved Miura-Ori pattern as shown in Fig. 11, row *1*. It can be seen that the shearing transformation removes reflection symmetry about the vertical direction in the pattern, which translates into anisotropic membrane and bending stiffness.

Poisson's Ratio. For all patterns we considered, folding leads to in-plane compression in all directions—in the sense that the folded sheet projected on its midplane exhibits uniformly shorter distances than in the flat state. Consequently, stretching the folded sheet will usually promote unfolding and therefore increase lengths in all directions, albeit to varying extents. This behavior leads to a negative in-plane Poisson ratio, as confirmed for all examples in Figs. 9—11.

For homogeneous elastic plates, a *negative* Poisson ratio in stretching would normally imply a tendency to develop *positive* Gaussian curvature when bent: curvature imposed in one direction is accompanied by curvature of the same sign in the orthogonal direction. By contrast, all origami patterns we analyzed predominantly produce negative Gaussian curvature under bending. This apparent discrepancy, already noted in previous work [Schenk and Guest 2010], arises from the fact that origami sheets are not continuous materials. Their mechanism-like architecture enables geometric modes of deformation that are far richer than those captured by classical plate theory, thereby decoupling the in-plane and out-of-plane Poisson effects.

It is worth noting that, due to their mechanism-like behavior, the Poisson's ratio for origami materials can be large in magnitude.

[3] *Leafy* designs courtesy of Ekaterina Lukasheva.

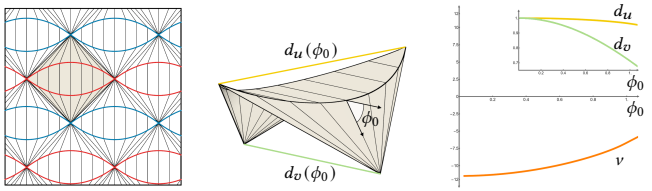

Fig. 6. Results for the theoretical validation of the Poisson ratio for the Huffman-inspired lens design shown in row *5* of Fig. 10. *Left*: Valid ruling assignment based on [Demaine et al. 2015]. *Middle*: Folded state of a cell of the pattern computed using numerical integration in *Mathematica*, illustrating the central fold angle ϕ_0. *Right*: Variation of distances d_u and d_v with increasing fold angle ϕ_0, with the corresponding Poisson ratio calculated as $\nu(\phi) = -d_v'/d_v \, (d_u'/d_u)^{-1}$.

There are several examples exhibiting values smaller than -1.0, indicating larger transverse than normal displacement during stretching. One extreme case is the Huffman-inspired lens pattern shown in Fig 10, row *5*, which exhibits a Poisson ratio close to -12.0. This unusually large (negative) value is explained by the fact that stretching the pattern in the horizontal direction straightens the concave lenses which, in turn, creates a strong lever that amplifies lateral displacement. Comparisons with an alternative isometry-based model confirm the predictions obtained from our homogenized model; see Fig. 6.

Straight vs. Curved Creases. Making general statements about the mechanical differences between straight-crease (SCO) and curved-crease origami (CCO) designs is not straightforward. Nevertheless, several of our examples exhibit direct correspondences between the two types, and some patterns even permit continuous transitions from straight to curved creases. Here we consider straight- and curved-crease versions of the Miura-ori pattern (Fig. 10, rows *7* and *8*) and Huffman's scaled parabolas (Fig. 10, rows *1* and *2*), as well as the sine-wave pattern (Fig. 5, rows *1* and *2*). These cases provide a basis for a few meaningful observations.

The minimum membrane stiffness of SCO designs is generally lower than that of the CCO counterparts, because SCO patterns admit deformation modes that promote unfolding without inducing facet bending. Nevertheless, membrane stiffness does not have to be uniformly lower than for the CCO version, as can be seen on the Miura-ori pattern.

For bending, SCO designs tend to be softer in all directions. The likely reason is that curved-crease patterns feature faces that are already bent in the folded state. Such pre-curved faces resist bending in orthogonal directions more strongly, since additional deformation would introduce double curvature, which is energetically costly. An exception to this trend is the special case of parallel straight creases (Fig. 10, row *6*), for which the maximum bending stiffness by far exceeds the largest value of the curved-crease version (Fig. 11, row *2*).

A practical advantage of curved-crease patterns is that their crease curvature can often be continuously tuned while preserving symmetry and foldability. We illustrate the impact of such curvature variation in Fig. 5. In contrast, straight-crease patterns are typically more restricted: even simple parameter modifications, such as nonuniform scaling or shearing of the unit cell, may violate foldability constraints and therefore cannot be used to adjust stiffness in a controlled manner.

Impact of Folding Magnitude. A general trend observed across all patterns is that membrane stiffness decreases, whereas bending stiffness increases, as the folding magnitude grows. In Fig. 4 we illustrate this behavior for four example patterns.

For the sine-wave pattern (*1st row*), the principal material directions remain fixed, but the stiffness magnitudes change substantially. While the material is initially almost five times stiffer along the horizontal axis, it becomes more than twice as stiff along the vertical axis in the most folded configuration—an axis inversion that also appears in the bending stiffness. This effect can be explained by the fact that even modest folding causes significant softening in the direction orthogonal to the creases, whereas the stiffness along the creases remains close to that of the base material. While additional folding has little effect on the already-softened vertical direction, it progressively reduces stiffness along the creases as they become increasingly curved.

As shown for the 3-fold symmetric spiral pattern (*2nd row*), isotropic materials remain isotropic throughout folding, and both membrane and bending stiffness vary monotonically with folding magnitude. The leaf pattern (*3rd row*) is initially nearly isotropic in its membrane response, but becomes increasingly stiffer along the vertical axis and therefore more orthotropic as folding progresses. Finally, the four-fold symmetric pattern (*4th row*) exhibits an interesting rotation of the principal material axes with varying folding magnitude. A possible explanation is that when considering the main crease lines of the pattern, we observe a slight rotation in orientation, particularly visible in the center of the pattern.

6.2 Centrosymmetry & Stretching-Bending Coupling

Symmetries in membrane and bending behaviors are determined by rotation and reflection symmetries of the crease pattern. However, this set of symmetries is insufficient to determine whether a material will show coupling between stretching and bending. As a necessary condition for a material to exhibit coupling between translational and rotational degrees of freedom, its structure must be non-centrosymmetric [Fernandez-Corbaton et al. 2019; Vasudevan and Pratapa 2024]. *Centrosymmetry* describes the symmetry of a structure under point inversion with respect to a given origin. Formally, a unit cell $\mathcal{U}$ is centrosymmetric if and only if there exists a point $\mathbf{x}_0$ (the *center of inversion*) such that

$$\forall\, \mathbf{x} \in \mathcal{U} \;\; \exists\, \mathbf{x}' \in \mathcal{U} \quad \text{with} \quad \mathbf{x}' = 2\mathbf{x}_0 - \mathbf{x}. \tag{34}$$

It is important to note that point inversion is fundamentally different from axis reflection and rotation. In two dimensions, centrosymmetry is equivalent to invariance under a rotation by 180°. However, this equivalence does not carry over to the three-dimensional setting of folded origami materials. Furthermore, invariance of a 2D crease pattern under 180° rotations does not imply centrosymmetry of the folded configuration—see examples below. To determine whether a

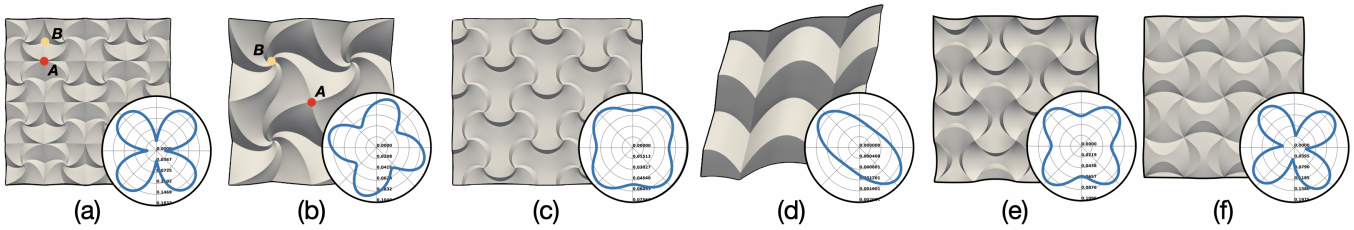

Fig. 7. Examples of non-centrosymmetric patterns and corresponding plots showing the magnitude of the curvature tensor induced by an imposed stretch in a given direction.

material can exhibit coupling between stretching and bending, we must test centrosymmetry on the folded pattern.

Numerical Detection of Centrosymmetry. In order to test an origami material for centrosymmetry, we evaluate the point-inversion condition numerically on the folded unit cell. To this end, we start by initializing the center of inversion $\mathbf{x}_0$ using the center of mass of the unit cell mesh and compute the point-reflected unit-cell mesh. For each vertex $\mathbf{y}_i$ of the reflected mesh, we compute the closest point $\mathbf{x}(\mathbf{y}_i)$ on the original unit-cell mesh, the corresponding distance $d_i = ||\mathbf{y}_i - \mathbf{x}(\mathbf{y}_i)||$, and the displacement vector $\mathbf{u}_i = \mathbf{y}_i - \mathbf{x}(\mathbf{y}_i)$. We then update the center of inversion as $\mathbf{x}_0 \leftarrow \mathbf{x}_0 + \mathbf{u}_{\text{avg}}$ using the average per-vertex displacement $\mathbf{u}_{\text{avg}}$. This procedure is repeated until $||\mathbf{u}_{\text{avg}}|| < \varepsilon_{\text{cs}}$, where $\varepsilon_{\text{cs}} = 10^{-5}$ is a threshold value. We conclude that a folded pattern is centrosymmetric if the average per-vertex distance $d_{\text{avg}} =< 10^{-1}L$, where L denotes the boundary length of the unit cell. Despite its simplicity, this fixed-point iteration converges rapidly (a few seconds for each of our examples) and reliably detects the presence or absence of centrosymmetry for all patterns considered.

Analyzing Patterns. We analyze our set of example patterns to verify that (*i*) centrosymmetry in 3D implies $\mathbf{B} \approx \mathbf{0}$ whereas $\mathbf{B} \neq \mathbf{0}$ requires non-centrosymmetry in 3D, (*ii*) materials with non-centrosymmetric folded states can have $\mathbf{B} \approx \mathbf{0}$, and (*iii*) centrosymmetric crease patterns can lead to non-centrosymmetric folded states.

(*i*) For all patterns that we investigated, we numerically verified that centrosymmetry of the folded state leads to absence of stretching-bending coupling with $\mathbf{B} \approx \mathbf{0}$. Conversely, all patterns for which the homogenized stiffness matrix satisfies $\mathbf{B} \neq \mathbf{0}$ have a non-centrosymmetric folded state. See Fig. 7 for an overview.

(*ii*) The fact that non-centrosymmetry in the folded state does not necessarily lead to coupling between stretching and bending can be seen on the curved Miura-ori pattern, for which we observe $\mathbf{B} \approx 0$. Interestingly, a sheared version of the curved Miura-ori pattern *does* lead to stretch-bending coupling (see Fig. 7*d*). This effect is arguably due to the fact that shearing the pattern reduces the symmetry of the folded state.

(*iii*) As a demonstration that 2D centrosymmetry does not imply 3D centrosymmetry we consider the two spiral patterns shown in Fig. 7*a* and *b*. It can be seen from Fig. 9, rows *4* and *7*, that the crease patterns for both examples exhibit four-fold rotational symmetry. Even though the crease patterns are thus centrosymmetric, their 3D folded states are not and the two materials exhibit distinct coupling. As a visual interpretation, the folded states have an intrinsic through-the-thickness asymmetry in which the two crease crossing points, labeled *A* and *B* in Fig. 7, are located on different sides of the midsurface. Since *A* and *B* have different valences and are therefore not equivalent, the structure cannot have point-inversion symmetry.

6.3 Exploring Pattern Parameters

Many of the designs that we explore in this work have parameters that can be changed continuously to modify the pattern and, consequently, the mechanical behavior of the folded origami materials. Curved crease patterns are particularly interesting in this context as crease curvature is a natural and easy to control parameter. Here, we consider two examples to highlight the range of effects on mechanical behavior that these parameter changes enable.

The first example is a curved-crease design consisting of stacked sine waves as shown in Fig. 5. We consider four variations of this pattern with increasing wave amplitude. With zero amplitude, the pattern reduces to the well-known and widely-used straight-crease variant with its sharp directional contrast in stretching and bending stiffness (row *1*). With increasing amplitude (row *2*), the membrane stiffness remains highest in the horizontal direction, but starts to soften. At the same time, membrane stiffness in the vertical direction is increasing. An analogous trend is observed for the bending stiffness. Ultimately, the vertical direction becomes dominant for both membrane and bending stiffness (row *4*). This parameter variation thus allows for continuous control of relative stiffness along principal axes.

Another example is the curved squares pattern of rows *5* and *6* in Fig. 9, where higher crease curvature leads to higher stiffness contrast. Interestingly, as shown in Fig. 7 columns *5* and *6*, a larger curvature parameter also leads to higher non-centrosymmetry and consequently stronger coupling between stretching and bending.

6.4 Comparing Simulations & Physical Prototypes

Prototype Fabrication. Given a periodic crease pattern with mountain-valley assignments, we create a sufficiently large patch by tiling the plane with at least 3×3 cells. For our physical prototypes, we use tear-resistant *Enduro Ice 135 paper*[4] with a weight of $141 g/m^2$. The crease lines are perforated using a laser cutter, after which the pattern is folded manually. The quasi-inextensible

[4]https://sihl.com/produkte/enduro-ice-135/

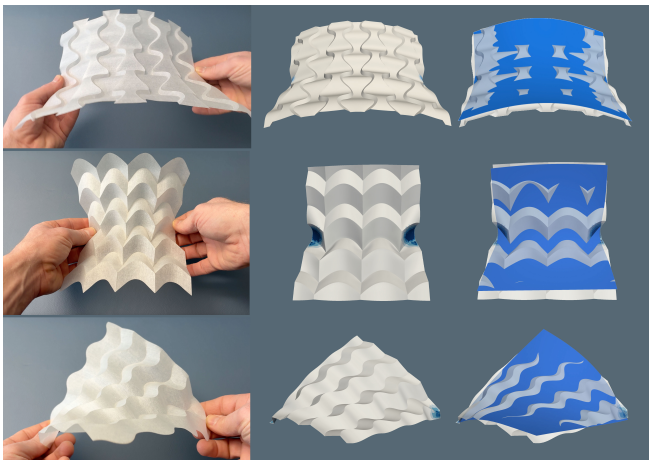

Fig. 8. Comparison between physical prototypes (*left*), native-scale simulations (*middle*) and homogenized simulations (*right*), shown as *light blue* overlays. Regions with applied boundary conditions are highlighted in *dark blue*.

material exhibits good elasticity for moderate deformations and comparatively high plasticity for creases. This combination leads to stable origami sheets that can undergo substantial deformations yet reliably return to their intended folded configuration.

Comparison. To evaluate our homogenized models, we incorporate the corresponding energy densities into a discrete-shell simulation based on a triangle-centered discretization of the shape operator. This simulation method is identical to the one used for native-scale folding and for the homogenization procedure itself; however, instead of applying it to periodic unit-cell samples, we now use it on finite-sized sheets. Applying periodic boundary conditions to the physical prototypes would be both impractical and undesirable. Such constraints would suppress the emergence of double-curvature configurations, which are a defining characteristic of our origami sheets and essential for capturing their full mechanical behavior.

When manipulating the prototypes, it becomes clear that some deformations are easy to induce while others are hard—sometimes because the response of the sheet is very stiff, but often because the material *escapes* into a different deformation mode; see also accompanying video. We therefore perform two sets of experiments: we bend the prototypes in a given soft direction and observe the curvature in the orthogonal direction. In the second set of tests we apply stretching in given directions and observe the resulting deformations—stretching and bending—in other directions. We then compare these observations to predictions obtained with our homogenized simulation. To mimic the types of manipulations that we apply to the physical prototypes, we set up spatially-averaged soft constraints to prescribe target locations for mesh vertices in regions where manipulation forces were applied in the real-world experiment.

As shown in Fig. 8, the homogenized simulations closely track the mid-surface geometry of the corresponding native-scale simulations. In addition, the simulated responses exhibit good qualitative agreement with the physical prototypes, reproducing key features such as double curvature and torsional deformation. We note, however, that differences in experimental conditions, along with discrepancies between the simulation meshes and the prototype boundary geometries, make more detailed comparisons difficult. Despite these limitations, the experiments provide encouraging evidence that both native-scale and homogenized models capture the essential mechanical behavior—we leave a comprehensive quantitative assessment for future work.

6.5 Performance & Statistics

Depending on the geometric complexity of the crease pattern, our unit-cell meshes contain between 1,100 and 22,000 vertices. A single step of the folding simulation requires approximately 1.2 s to 22.4 s, and full folding trajectories typically complete within 5 to 55 minutes. Homogenization involves solving six linear systems with an identical coefficient matrix, making its computational cost negligible compared to computing the folded configuration. All timings were collected on an Apple Macbook Pro (2021) with M1 Max CPUs.

For comparisons between native-scale and homogenized simulations, we tile the unit cell into a 3×3 patch, yielding meshes with roughly $45k$ triangles. Native-scale simulations on these meshes take about $40s$ per step, whereas homogenized simulations on meshes with around $1k$ triangles require only about $0.2s$ per step.

Fabricating and folding the physical prototypes is significantly more time-consuming and requires expert handling. Depending on the size and geometric complexity of a design, the initial folding process took up to a few hours.

7 Conclusions

We presented a unified computational framework that combines simulation-based folding with numerical homogenization to predict the effective mechanical behavior of periodic origami materials. Treating straight and curved creases in a unified way allowed us to study how crease shape and pattern symmetry govern macromechanical stretching and bending responses, as well as their coupling. By enabling systematic exploration of geometric parameters, our method sheds light on how folding magnitude and crease curvature impact emergent material behavior. The resulting homogenized models show good agreement with native scale simulations and qualitatively reproduce deformation responses observed in experimental prototypes.

Limitations and Future Work. A natural extension of our work is to replace the quadratic energy formulation with a fully nonlinear simulation framework for homogenization, enabling the derivation of corresponding nonlinear constitutive laws. Such a model would make it possible to capture effects such as buckling, bistability, and stiffness changes caused by internal contacts—which we do not currently handle—or geometric nonlinearities.

Our proposed folding algorithm yields energetically optimal folded states with substantially lower isometry violations compared to existing alternatives. Nevertheless, more complex designs may still exhibit non-negligible in-plane deformations—up to 4% near the centers of the spiral patterns shown in Fig. 9, row *4*.

While increasing mesh resolution may help reduce stretching, we hypothesize that the dominant source is a locking-like artifact associated with linear triangle finite elements. Future work should therefore investigate the use of higher-order elements to assess whether quasi-developable behavior can be achieved even in such challenging configurations.

Our current homogenization framework relies on a non-periodic torsion field to probe the double curvature response of origami sheets. As a result, the effective behavior depends on the chosen unit-cell size, particularly regarding the coupling of curvature in different directions. Future work could explore alternative displacement fields that exhibit double curvature while remaining periodic at their boundaries.

Our prototype evaluations are qualitative, and we do not claim quantitative accuracy in the predicted stiffness values. A rigorous experimental characterization of these material properties would be valuable, although challenging due to the need to control and capture the full state of curvature and in-plane deformation.

We investigated the influence of folding magnitude through simulation and found that this parameter can lead to significant and meaningful variations in the mechanical response. However, accurately controlling the folding magnitude in our manually fabricated prototypes is challenging. To reliably validate these predictions, additional experiments using automated fabrication methods, such as 3D printing or other techniques that enable precise control of fold angles, should be conducted.

Inverse design methods represent another exciting direction, with the potential to further unlock origami as a rich design space for programmable plate-like materials.

While our focus has been on crease patterns that fold into flat configurations, many patterns produce cylindrical or even spherical curvature when folded. A deeper understanding of how a pattern's topology and geometry govern its resulting curvature would be valuable for designing origami surfaces with user-specified shapes.

Finally, we see considerable promise in exploring spatially varying crease patterns, which could enable materials with locally tailored mechanical responses and complex, smoothly varying target geometries.

Acknowledgments

We would like to thank the reviewers for their valuable feedback. This work was supported by the Swiss National Science Foundation through SNF project grants 200021-236469 and 200021-231293.

A Optimal Deformations and Stiffness

For a given direction α, we compute the energetically optimal state of deformation $\mathbf{s} = (\varepsilon_{xx}, \ldots, \kappa_{xy})^T$ by solving the optimization problem

$$\min_{\mathbf{s}} \ \frac{1}{2}\mathbf{s}^T\mathbf{K}\mathbf{s} \quad \text{s.t} \quad \mathbf{c}^T\mathbf{s} - \beta = 0 \,. \tag{35}$$

The Lagrangian for this problem is

$$\mathcal{L}(\mathbf{s}, \lambda) = \frac{1}{2}\mathbf{s}^T\mathbf{K}\mathbf{s} + \lambda(\mathbf{c}^T\mathbf{s} - \beta) \,, \tag{36}$$

where λ is a Lagrange multiplier for the single constraint. The first-order optimality conditions require that the gradient of $\mathcal{L}$ vanish with respect to both $\mathbf{s}$ and λ, i.e.,

$$\nabla_{\mathbf{s}}\mathcal{L} = \mathbf{K}\mathbf{s} + \lambda\mathbf{c} = \mathbf{0} \,, \tag{37}$$

$$\nabla_{\lambda}\mathcal{L} = \mathbf{c}^T\mathbf{s} - \beta = 0 \,. \tag{38}$$

Solving for the unknown $\mathbf{s}$ and λ leads to a set of linear equations,

$$\begin{bmatrix} \mathbf{K} & \mathbf{c} \\ \mathbf{c}^T & \mathbf{0} \end{bmatrix} \begin{bmatrix} \mathbf{s} \\ \lambda \end{bmatrix} = \begin{bmatrix} \mathbf{0} \\ \beta \end{bmatrix} \,. \tag{39}$$

From the first row, we obtain $\mathbf{s} = -\mathbf{K}^{-1}\mathbf{c}\lambda$ which, when inserted into the second row, yields $\lambda = -(\mathbf{c}^T\mathbf{K}^{-1}\mathbf{c})^{-1}\beta$. Plugging this expression for λ back into the first row, we obtain

$$\mathbf{s} = -\mathbf{K}^{-1}\mathbf{c}\lambda = \mathbf{K}^{-1}\mathbf{c}(\mathbf{c}^T\mathbf{K}^{-1}\mathbf{c})^{-1}\beta \,. \tag{40}$$

References

Katia Bertoldi, Vincenzo Vitelli, Johan Christensen, and Martin Van Hecke. 2017. Flexible mechanical metamaterials. *Nature Reviews Materials* 2, 11 (2017), 1–11.

Bernd Bickel, Moritz Bächer, Miguel A Otaduy, Hyunho Richard Lee, Hanspeter Pfister, Markus Gross, and Wojciech Matusik. 2010. Design and fabrication of materials with desired deformation behavior. *ACM Transactions on Graphics (TOG)* 29, 4 (2010), 1–10.

Sibo Chai, Zhou Hu, Yan Chen, Zhong You, and Jiayao Ma. 2024. Programmable multistability of curved-crease origami structures with travelling folds. *Journal of the Mechanics and Physics of Solids* 193 (2024), 105877.

Erik D Demaine, Martin L Demaine, David A Huffman, Duks Koschitz, and Tomohiro Tachi. 2015. Characterization of curved creases and rulings: Design and analysis of lens tessellations. *Origami* 6 (2015), 209–230.

Erik D. Demaine, Martin L. Demaine, David A. Huffman, Duks Koschitz, and Tomohiro Tachi. 2018. Conic Crease Patterns with Reflecting Rule Lines. In *Origami^7: Proceedings of the 7th International Meeting on Origami in Science, Mathematics and Education (OSME 2018)*. Vol. 2. Tarquin, Oxford, England, 573–590.

Erik D Demaine, Martin L Demaine, and Duks Koschitz. 2011. Reconstructing David Huffman's legacy in curved-crease folding. *Origami* 5 (2011), 39–52.

Levi H. Dudte, Etienne Vouga, Tomohiro Tachi, and L. Mahadevan. 2016. Programming curvature using origami tessellations. *Nature Materials* 15 (5 2016), 583–588. Issue 5. https://doi.org/10.1038/nmat4540

Simon Dünser, Bernhard Thomaszewski, Roi Poranne, and Stelian Coros. 2022. Nonlinear Compliant Modes for Large-deformation Analysis of Flexible Structures. *ACM Trans. Graph.* 42, 2, Article 21 (Nov. 2022), 11 pages. https://doi.org/10.1145/3568952

Xudong Feng, Huamin Wang, Yin Yang, and Weiwei Xu. 2024. Neural-Assisted Homogenization of Yarn-Level Cloth. In *ACM SIGGRAPH 2024 Conference Papers* (Denver, CO, USA) *(SIGGRAPH '24)*. Association for Computing Machinery, New York, NY, USA, Article 80, 10 pages. https://doi.org/10.1145/3641519.3657411

I. Fernandez-Corbaton, C. Rockstuhl, P. Ziemke, P. Gumbsch, A. Albiez, R. Schwaiger, T. Frenzel, M. Kadic, and M. Wegener. 2019. New Twists of 3D Chiral Metamaterials. *Advanced Materials* 31, 26 (2019), 1807742. https://doi.org/10.1002/adma.201807742 arXiv:https://advanced.onlinelibrary.wiley.com/doi/pdf/10.1002/adma.201807742

Amanda Ghassaei, Erik D Demaine, and Neil Gershenfeld. 2018. Fast, interactive origami simulation using GPU computation. *Origami* 7 (2018), 1151–1166.

Eitan Grinspun, Yotam Gingold, Jason Reisman, and Denis Zorin. 2006. Computing discrete shape operators on general meshes. *Computer Graphics Forum* 25, 3 (2006), 547–556. https://doi.org/10.1111/j.1467-8659.2006.00974.x arXiv:https://onlinelibrary.wiley.com/doi/pdf/10.1111/j.1467-8659.2006.00974.x

Eitan Grinspun, Anil N. Hirani, Mathieu Desbrun, and Peter Schröder. 2003. Discrete Shells. In *Symposium on Computer Animation*, D. Breen and M. Lin (Eds.). The Eurographics Association. https://doi.org/10.2312/SCA03/062-067

Ruslan Guseinov, Eder Miguel, and Bernd Bickel. 2017. CurveUps: shaping objects from flat plates with tension-actuated curvature. *ACM Trans. Graph.* 36, 4, Article 64 (July 2017), 12 pages. https://doi.org/10.1145/3072959.3073709

Siyuan He, Meng-Jan Wu, Arthur Lebée, and Mélina Skouras. 2025. MatAIRials: Isotropic Inflatable Metamaterials for Freeform Surface Design. *Computer Graphics Forum* 44, 5 (2025), e70190. https://doi.org/10.1111/cgf.70190 arXiv:https://onlinelibrary.wiley.com/doi/pdf/10.1111/cgf.70190

Rodney Hill. 1963. Elastic properties of reinforced solids: some theoretical principles. *Journal of the Mechanics and Physics of Solids* 11, 5 (1963), 357–372.

Mohammad Jahedol Islam, Bin Bao, and Fujun Peng. 2025. Recent developments of mechanical metamaterials inspired by origami: from methodologies, fabrication to challenges. *Applied Materials Today* 44 (2025), 102715. https://doi.org/10.1016/j.apmt.2025.102715

David Jourdan, Mélina Skouras, Etienne Vouga, and Adrien Bousseau. 2022. Computational Design of Self-Actuated Surfaces by Printing Plastic Ribbons on Stretched Fabric. In *Computer Graphics Forum*, Vol. 41. Wiley Online Library, 493–506.

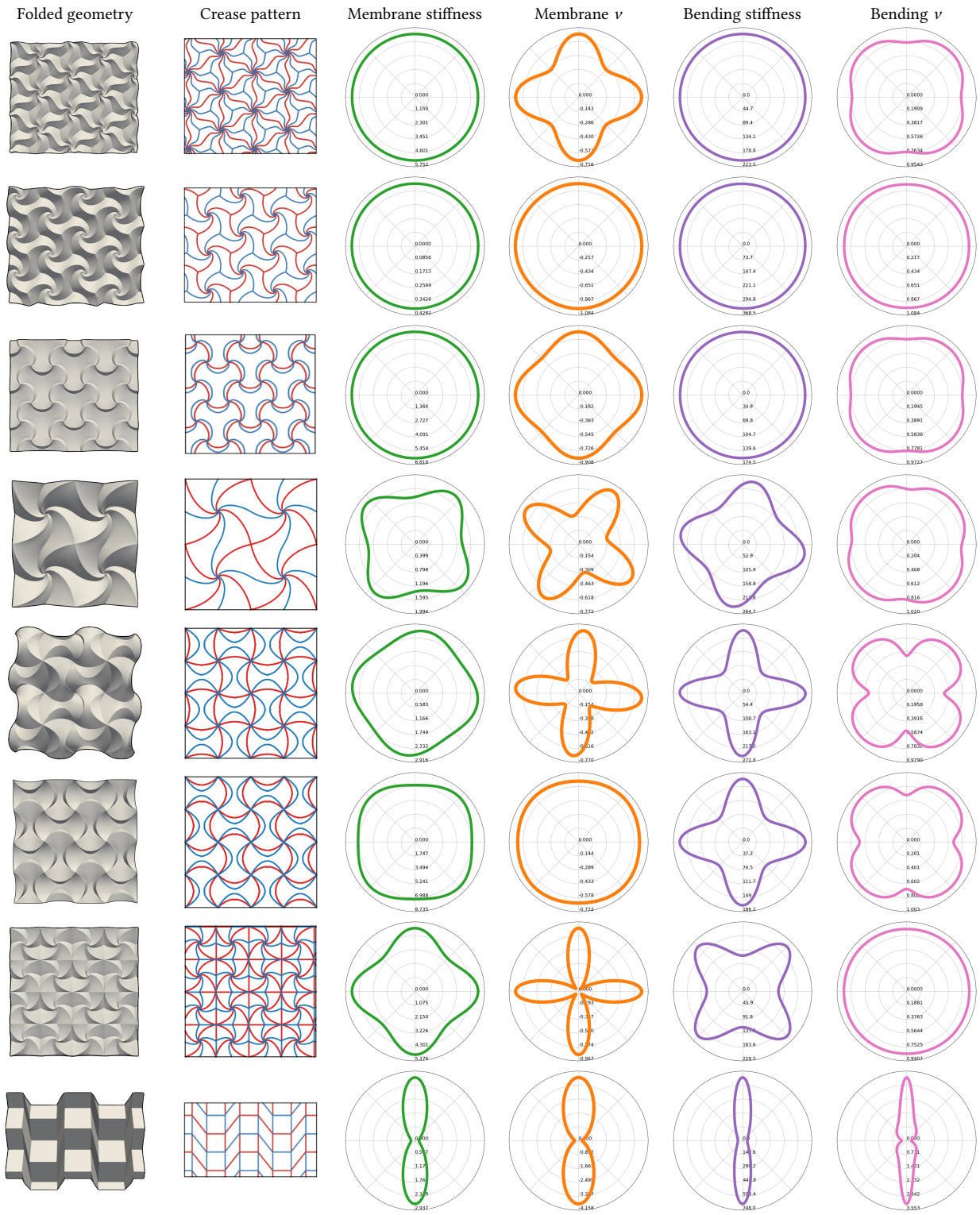

Fig. 9. Overview of homogenization results, *part 1*. From *left* to *right*: folded geometry snapshot, crease pattern with mountain-valley assignment in blue/red, polar plots of membrane stiffness, membrane Poisson ratio, bending stiffness, and bending Poisson ratio.

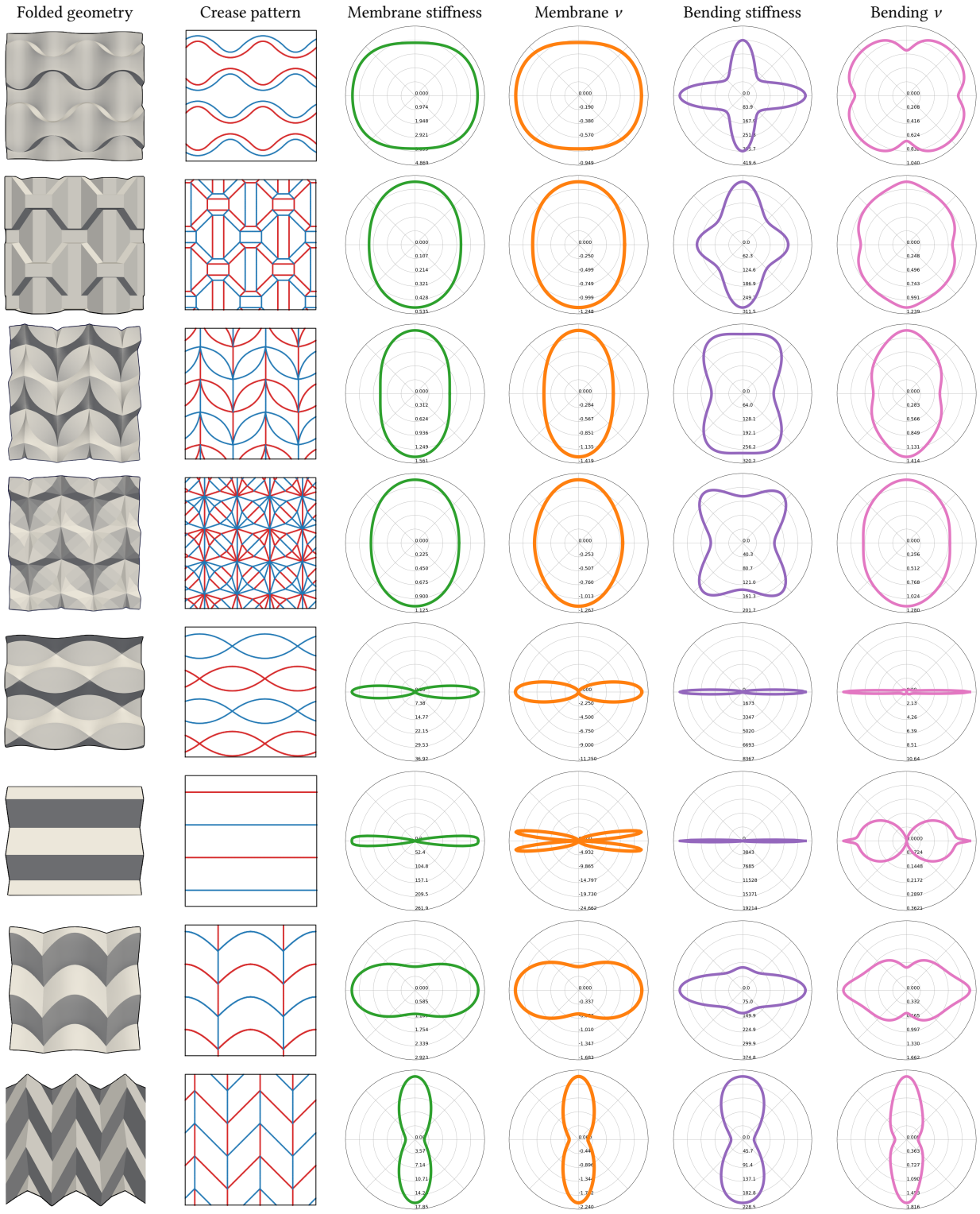

Fig. 10. Overview of homogenization results, *part 2*. From *left* to *right*: folded geometry snapshot, crease pattern with mountain-valley assignment in blue/red, polar plots of membrane stiffness, membrane Poisson ratio, bending stiffness, and bending Poisson ratio.

Asma Karami, Adam Reddy, and Hussein Nassar. 2024. Curved-Crease Origami for Morphing Metamaterials. *Physical Review Letters* 132 (3 2024). Issue 10. https://doi.org/10.1103/PhysRevLett.132.108201

Martin Kilian, Simon Flöry, Zhonggui Chen, Niloy J Mitra, Alla Sheffer, and Helmut Pottmann. 2008. Curved folding. *ACM transactions on graphics (TOG)* 27, 3 (2008), 1–9.

Martin Kilian, Aron Monszpart, and Niloy J Mitra. 2017. String actuated curved folded surfaces. *ACM Transactions on Graphics (TOG)* 36, 3 (2017), 1–13.

Mina Konaković, Keenan Crane, Bailin Deng, Sofien Bouaziz, Daniel Piker, and Mark Pauly. 2016. Beyond developable: computational design and fabrication with auxetic materials. *ACM Trans. Graph.* 35, 4, Article 89 (July 2016), 11 pages. https://doi.org/10.1145/2897824.2925944

Mina Konaković-Luković, Julian Panetta, Keenan Crane, and Mark Pauly. 2018. Rapid Deployment of Curved Surfaces via Programmable Auxetics. *ACM Trans. Graph.* 37, 4, Article 106 (July 2018), 13 pages. https://doi.org/10.1145/3197517.3201373

Miura Koryo. 1985. Method of packaging and deployment of large membranes in space. *The Institute of Space and Astronautical Science report* 618 (1985), 1–9.

Richard Duks Koschitz. 2014. *Computational design with curved creases: David Huffman's approach to paperfolding.* Ph. D. Dissertation. Massachusetts Institute of Technology.

Robert J Lang. 2017. *Twists, tilings, and tessellations: Mathematical methods for geometric origami.* AK Peters/CRC Press.

Winnie Leung and Ilan Garibi. 2024. *Fold & Explore Curved Origami Tessellations.*

Suyi Li, Hongbin Fang, Sahand Sadeghi, Priyanka Bhovad, and Kon-Well Wang. 2019. Architected Origami Materials: How Folding Creates Sophisticated Mechanical Properties. *Advanced Materials* 31, 5 (2019), 1805282. https://doi.org/10.1002/adma.201805282 arXiv:https://advanced.onlinelibrary.wiley.com/doi/pdf/10.1002/adma.201805282

Yue Li, Stelian Coros, and Bernhard Thomaszewski. 2023. Neural Metamaterial Networks for Nonlinear Material Design. *ACM Trans. Graph.* 42, 6, Article 186 (dec 2023), 13 pages. https://doi.org/10.1145/3618325

Huan Liu and Richard D. James. 2025. Foldable piecewise linear origami that approximates curved tile origami. *Journal of the Mechanics and Physics of Solids* 195 (2025), 105962. https://doi.org/10.1016/j.jmps.2024.105962

Ekaterina Lukasheva. 2021. *Curved Origami.*

Cheng Lv, Deepakshyam Krishnaraju, Goran Konjevod, Hongyu Yu, and Hanqing Jiang. 2014. Origami based mechanical metamaterials. *Scientific Reports* 4 (8 2014). https://doi.org/10.1038/srep05979

J Mandel. 1971. Plasticité classique et viscoplasticité (CISM Lecture notes, Udine, Italy).

Jonàs Martínez, Jérémie Dumas, and Sylvain Lefebvre. 2016. Procedural voronoi foams for additive manufacturing. *ACM Transactions on Graphics (TOG)* 35, 4 (2016), 1–12.

Jonàs Martínez, Mélina Skouras, Christian Schumacher, Samuel Hornus, Sylvain Lefebvre, and Bernhard Thomaszewski. 2019. Star-shaped metrics for mechanical metamaterial design. *ACM Transactions on Graphics (TOG)* 38, 4 (2019), 1–13.

Jonàs Martínez, Haichuan Song, Jérémie Dumas, and Sylvain Lefebvre. 2017. Orthotropic k-nearest foams for additive manufacturing. *ACM Transactions on Graphics (TOG)* 36, 4 (2017), 1–12.

Marco Meloni, Jianguo Cai, Qian Zhang, Daniel Sang-Hoon Lee, Meng Li, Ruijun Ma, Teo Emilov Parashkevov, and Jian Feng. 2021. Engineering Origami: A Comprehensive Review of Recent Applications, Design Methods, and Tools. *Advanced Science* 8, 13 (2021), 2000636. https://doi.org/10.1002/advs.202000636 arXiv:https://advanced.onlinelibrary.wiley.com/doi/pdf/10.1002/advs.202000636

Jun Mitani. 2019. *Curved-folding origami design.* CRC Press.

Juan Sebastian Montes Maestre, Yinwei Du, Ronan Hinchet, Stelian Coros, and Bernhard Thomaszewski. 2024. FlexScale: Modeling and Characterization of Flexible Scaled Sheets. *ACM Trans. Graph.* 43, 4, Article 86 (July 2024), 14 pages. https://doi.org/10.1145/3658175

Hussein Nassar, Arthur Lebée, Laurent Monasse, H Nassar, A Lebée, and L Monasse. 2017. Curvature, metric and parametrization of origami tessellations: Theory and application to the eggbox pattern. *Proceedings of the Royal Society of Edinburgh: Section A, Mathematics* 473 (2017). https://doi.org/10.1098/rspa.2016.0705Ãŕ

Julian Panetta, Florin Isvoranu, Tian Chen, Emmanuel Siéfert, Benoît Roman, and Mark Pauly. 2021. Computational inverse design of surface-based inflatables. *ACM Trans. Graph.* 40, 4, Article 40 (July 2021), 14 pages. https://doi.org/10.1145/3450626.3459789

Julian Panetta, Qingnan Zhou, Luigi Malomo, Nico Pietroni, Paolo Cignoni, and Denis Zorin. 2015. Elastic textures for additive fabrication. *ACM Transactions on Graphics (TOG)* 34, 4 (2015), 1–12.

Jesús Pérez, Miguel A. Otaduy, and Bernhard Thomaszewski. 2017. Computational design and automated fabrication of kirchhoff-plateau surfaces. *ACM Trans. Graph.* 36, 4, Article 62 (July 2017), 12 pages. https://doi.org/10.1145/3072959.3073695

Michael Rabinovich, Tim Hoffmann, and Olga Sorkine-Hornung. 2019. Modeling curved folding with freeform deformations. *ACM Transactions on Graphics* 38 (11 2019). Issue 6. https://doi.org/10.1145/3355089.3356531

J.N. Reddy. 2003. *Mechanics of Laminated Composite Plates and Shells: Theory and Analysis, Second Edition.* CRC Press.

Yingying Ren, Julian Panetta, Seiichi Suzuki, Uday Kusupati, Florin Isvoranu, and Mark Pauly. 2024. Computational Homogenization for Inverse Design of Surface-based Inflatables. *ACM Trans. Graph.* 43, 4, Article 87 (July 2024), 18 pages. https://doi.org/10.1145/3658125

Géry Saxcé and Claude Vallée. 2013. Invariant measures of the lack of symmetry with respect to the symmetry groups of 2D elasticity tensors. *Journal of Elasticity* 1, 111 (2013), 21–39.

Mark Schenk and Simon D Guest. 2010. Folded textured sheets. In *Symposium of the International Association for Shell and Spatial Structures (50th. 2009. Valencia). Evolution and Trends in Design, Analysis and Construction of Shell and Spatial Structures: Proceedings.* Editorial Universitat Politècnica de València.

Mark Schenk and Simon D. Guest. 2013. Geometry of Miura-folded metamaterials. *Proceedings of the National Academy of Sciences* 110, 9 (2013), 3276–3281. https://doi.org/10.1073/pnas.1217998110 arXiv:https://www.pnas.org/doi/pdf/10.1073/pnas.1217998110

Christian Schumacher, Bernd Bickel, Jan Rys, Steve Marschner, Chiara Daraio, and Markus Gross. 2015. Microstructures to control elasticity in 3D printing. *ACM Transactions on Graphics (Tog)* 34, 4 (2015), 1–13.

Christian Schumacher, Steve Marschner, Markus Gross, and Bernhard Thomaszewski. 2018. Mechanical characterization of structured sheet materials. *ACM Transactions on Graphics (TOG)* 37, 4 (2018), 1–15.

Georg Sperl, Rahul Narain, and Chris Wojtan. 2020. Homogenized yarn-level cloth. *ACM Trans. Graph.* 39, 4 (2020), 48.

Yucong Sun, Keyao Song, Jaehyung Ju, and Xiang Zhou. 2024. Curved-creased origami mechanical metamaterials with programmable stabilities and stiffnesses. *International Journal of Mechanical Sciences* 262 (1 2024). https://doi.org/10.1016/j.ijmecsci.2023.108729

Kai Suto, Yuta Noma, Kotaro Tanimichi, Koya Narumi, and Tomohiro Tachi. 2023. Crane: an integrated computational design platform for functional, foldable, and fabricable origami products. *ACM Transactions on Computer-Human Interaction* 30, 4 (2023), 1–29.

Tomohiro Tachi. 2010. Freeform Variations of Origami. *Journal of Geometry and Graphics* 14 (2010), 203–215.

Chengcheng Tang, Pengbo Bo, Johannes Wallner, and Helmut Pottmann. 2016. Interactive design of developable surfaces. *ACM Transactions on Graphics (TOG)* 35, 2 (2016), 1–12.

Pengbin Tang, Stelian Coros, and Bernhard Thomaszewski. 2023. Beyond Chainmail: Computational Modeling of Discrete Interlocking Materials. *ACM Trans. Graph.* 42, 4, Article 84 (July 2023), 12 pages. https://doi.org/10.1145/3592112

Pengbin Tang, Ronan Hinchet, Roi Poranne, Bernhard Thomaszewski, and Stelian Coros. 2024. Modal Folding: Discovering Smooth Folding Patterns for Sheet Materials using Strain-Space Modes. In *ACM SIGGRAPH 2024 Conference Papers* (Denver, CO, USA) *(SIGGRAPH '24).* Association for Computing Machinery, New York, NY, USA, Article 48, 9 pages. https://doi.org/10.1145/3641519.3657401

Davi Colli Tozoni, Jérémie Dumas, Zhongshi Jiang, Julian Panetta, Daniele Panozzo, and Denis Zorin. 2020. A low-parametric rhombic microstructure family for irregular lattices. *ACM Transactions on Graphics (TOG)* 39, 4 (2020), 101–1.

Siva P. Vasudevan and Phanisri P. Pratapa. 2024. Homogenization of non-rigid origami metamaterials as Kirchhoff–Love plates. *International Journal of Solids and Structures* 300 (2024), 112929. https://doi.org/10.1016/j.ijsolstr.2024.112929

Z. Y. Wei, Z. V. Guo, L. Dudte, H. Y. Liang, and L. Mahadevan. 2013. Geometric mechanics of periodic pleated origami. *Physical Review Letters* 110 (5 2013). Issue 21. https://doi.org/10.1103/PhysRevLett.110.215501

Steven Woodruff. 2022. *How curved creases enhance the stiffness and enable shape morphing of thin-sheet structures.* Ph. D. Dissertation.

Steven R Woodruff and Evgueni T Filipov. 2021. Curved creases redistribute global bending stiffness in corrugations: theory and experimentation. *Meccanica* 56, 6 (2021), 1613–1634.

IM Zakirov and KA Alekseyev. 2004. Shaping of folded single-curvature cores. In *Proceedings of the all-union scientific-practical conference on aerospace technologies and equipment, Kazan.* 5–9.

Zirui Zhai, Lingling Wu, and Hanqing Jiang. 2021. Mechanical metamaterials based on origami and kirigami. *Applied Physics Reviews* 8, 4 (2021).

Zhan Zhang, Christopher Brandt, Jean Jouve, Yue Wang, Tian Chen, Mark Pauly, and Julian Panetta. 2023. Computational Design of Flexible Planar Microstructures. *ACM Trans. Graph.* 42, 6, Article 185 (dec 2023), 16 pages. https://doi.org/10.1145/3618396

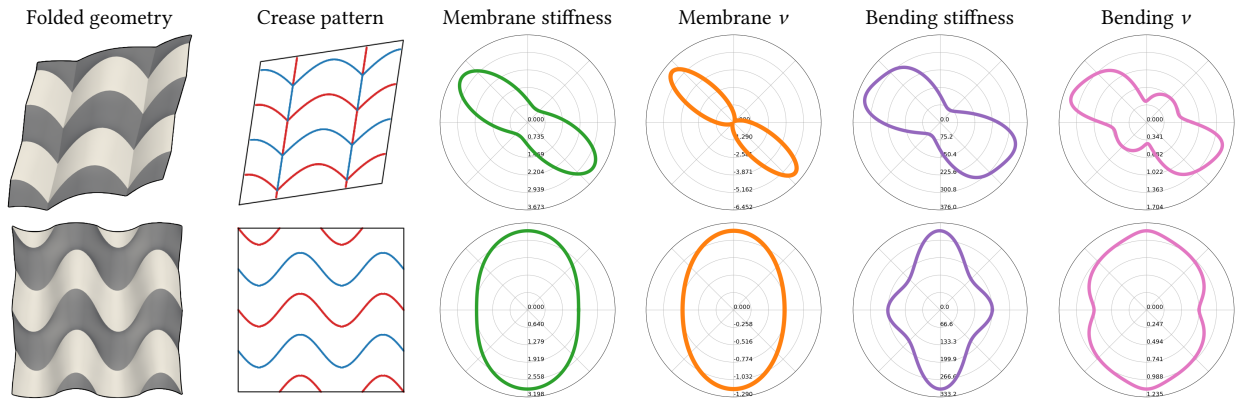

Fig. 11. Overview of homogenization results, *part 3*. From *left* to *right*: folded geometry snapshot, crease pattern with mountain-valley assignment in blue/red, polar plots of membrane stiffness, membrane Poisson ratio, bending stiffness, and bending Poisson ratio.